Check for updates

View Article Online
View Journal

PCCP
Physical Chemistry Chemical Physics

Accepted Manuscript

This article can be cited before page numbers have been issued, to do this please use: A. H. Reksten, A. E. Russell, P. W. Richardson, S. J. Thompson, K. Mathisen, F. Seland and S. Sunde, *Phys. Chem. Chem. Phys.*, 2020, DOI: 10.1039/D0CP00217H.

This is an Accepted Manuscript, which has been through the Royal Society of Chemistry peer review process and has been accepted for publication.

Accepted Manuscripts are published online shortly after acceptance, before technical editing, formatting and proof reading. Using this free service, authors can make their results available to the community, in citable form, before we publish the edited article. We will replace this Accepted Manuscript with the edited and formatted Advance Article as soon as it is available.

You can find more information about Accepted Manuscripts in the Information for Authors.

Please note that technical editing may introduce minor changes to the text and/or graphics, which may alter content. The journal's standard Terms & Conditions and the Ethical guidelines still apply. In no event shall the Royal Society of Chemistry be held responsible for any errors or omissions in this Accepted Manuscript or any consequences arising from the use of any information it contains.

ROYAL SOCIETY OF CHEMISTRY

rsc.li/pccp

View Article Online
DOI: 10.1039/D0CP00217H

Journal Name

ARTICLE TYPE

Cite this: DOI: 10.1039/xxxxxxxxxx

An in Situ XAS Study of High Surface-Area IrO_2 Produced by the Polymeric Precursor Synthesis†

Anita Hamar Reksten,[a‡] Andrea E. Russell,[b] Peter W. Richardson,[b] Stephen J. Thompson,[b] Karina Mathisen,[c] Frode Seland,[a] and Svein Sunde[d]

Received Date
Accepted Date

DOI: 10.1039/xxxxxxxxxx

www.rsc.org/journalname

Iridium oxide powders with a surface area of more than 1 $m^2\ g^{-1}$ (4 $m^2\ g^{-1}$ from the H-UPD charge) and iridium-oxide crystallites less than 10 nm across were synthesized by heat treating gels formed from citric acid, ethylene glycol and dihydrogen hexachloroiridate(IV) in air. The characteristics of the resulting material was found to be strongly dependent on the heat-treatment step in the synthesis. A single heat-treatment of the gel resulted in a material with a substantial fraction of elemental iridium metal, i.e. iridium in oxidation state zero (Ir^0). Post-synthesis modification of the powder by potential cycling resulted in oxidation peaks consistent with the conversion of the metal phase to iridium oxide. Linear combination of the near-edge part of the X-ray absorption data (X-ray absorbtion near-edge spectroscopy, XANES) collected in situ during potential cycling and an analysis of the extended X-ray fine-structure (EXAFS) part of the spectrum showed that the overall metal fraction was not significantly affected by the cycling. The oxidation of the metal phase is therefore limited to a thin layer of oxide at the metal surface, and a significant part of the iridium is left inactive. A modification of the heat treatment procedure of the sample resulted in iridium oxide containing only insignificant amounts of elemental iridium metal.

1 Introduction

Iridium oxide films play an important role in several practical applications such as supercapacitors[1–3], electrochromic materials[4], pH-electrodes[5–8] and oxygen-evolving catalysts[9,10]. Iridium oxide films can be formed electrochemically by pulsing or cycling the potential of a metallic iridium electrode between certain vertex potentials in aqueous solutions. The product is anodic iridium oxide films (AIROFs, in biological applications sometimes taken as an acronym for *activated* iridium oxide films[11]), which are hydrous and exhibit rapid oxidation/reduction kinetics when the film is switched between the Ir(+3) and Ir(+4) states. Unlike metallic ruthenium, which is readily oxidized at sufficiently high potential, at iridium electrodes pulsing or cycling the potential is a prerequisite for oxide growth to proceed beyond a thin compact layer[12].

Iridium oxide films may also be produced by a number of other methods, including physical methods such as sputtering[13], electrochemical deposition from solution precursors[14], and various chemical synthesis methods including the hydrolysis method[15–17], polymeric precursor synthesis (PPS)[18] and the Adams Fusion method[19–21]. Common to these different forms of iridium oxides is that they are all redox active. During redox cycling the oxides may therefore in general be expected to exchange protons, hydroxyl ions, other solution ions and water with the electrolyte solution, the ionic species compensating each other and the net electronic charge of the iridium oxide[22]. The voltammograms of iridium oxides prepared by the hydrolysis and Adams fusion methods are similar to those of AIROF, but frequently with substantially less well-resolved peaks. In some cases the oxides are electrochromic, i.e. their color changes with the state of charge (sputtered iridium oxides (SIROF)[23], AIROF[24,25], and electrochemically deposited iridium oxide (EIROF)[26]), in others not (hydrolysis)[27].

Changes in iridium valence in iridium oxide subjected to potential control in an electrochemical cell were demonstrated directly in X-ray absorption spectroscopy (XAS) studies of AIROF by Hüppauff and Lengeler[28]. They concluded that the oxidation state of Ir changes from +3 to +4.8 as the potential goes from −0.24 V to 1.21 V vs. Ag/AgCl by comparing the peak positions in voltammo-

[a] Department of Materials Science and Engineering, Norwegian University of Science and Technology (NTNU), NO-7491, Trondheim, Norway.
[b] Department of Chemistry, University of Southampton, Southampton SO17 1BJ, England.
[c] Department of Chemistry, Norwegian University of Science and Technology (NTNU), NO-7491 Trondheim, Norway.
[d] Department of Materials Science and Engineering, Norwegian University of Science and Technology (NTNU), NO-7491, Trondheim, Norway. Fax: +47 7359 1105; Tel: +47 7359 4051; E-mail: svein.sunde@ntnu.no

† Electronic Supplementary Information (ESI) available: [details of any supplementary information available should be included here]. See DOI: 10.1039/b000000x/

‡ Current address: SINTEF Sustainable Energy Technology, NO-0373 Oslo, Norway.

Published on 30 March 2020. Downloaded by University of Southampton on 3/31/2020 1:02:17 PM.

Physical Chemistry Chemical Physics Accepted Manuscript

View Article Online
DOI: 10.1039/D0CP00217H

Published on 30 March 2020. Downloaded by University of Southampton on 3/31/2020 1:02:17 PM.

grams for the oxides with those of reference compounds. Similar results for sputtered and electrochemically deposited films were obtained by Pauporté *et al.* [13] and Hillman *et al.* [14], respectively.

Electrochemical treatment of electrocatalyst structures sometimes plays an important role in the synthesis of catalysts, for example through rearrangement of the atomic structure of precursor particles of the catalyst with or without concomitant changes in their oxidation state [29–31]. During initial characterization of iridium oxides prepared by polymeric precursor synthesis [32] significant changes in the voltammograms from cycle to cycle were observed. The voltammograms were initially rather broad and featureless, but sharp peaks emerged after a certain number of potential cycles in a fashion quite similar to how voltammograms change from cycle to cycle during growth of AIROF [33]. Oxides prepared by the PPS may contain significant fractions of metal [34–40], and it is therefore natural to conjecture that the film contained elemental iridium metal, i.e iridium in oxidation state zero Ir^0, gradually being converted to an AIROF-like oxide. However, to which extent this happens and in which ways potential cycling alters any other of the oxide-metal composite also structurally is unclear, however.

Any elemental iridium metal in the oxides may affect the overall catalytic activity of the composite. If the elemental metal content changes during electrochemical characterization this will compromise the analysis, leaving the experimental conditions ill-defined and to irreproducible results. It is therefore vital for any research on the PPS method of synthesis to establish well-defined experimental conditions for the characterization. Finally, it is of great interest to establish in which way and to which extent it is possible to treat iridium oxide prepared through PPS electrochemically to optimize its properties as an efficient oxygen-evolution catalyst. The works of Pauporté [13], Hillman [14] and Hüppauff and Lengeler [28] indicate that XAS measurements are well suited to address the question as to whether electrochemical post-treatment can be expected to transform the material into an oxide throughout in such cases.

Below we report characterization of elemental metal-containing oxides obtained by the PPS used to produce catalyst powders [32] for the oxygen-evolution reaction (OER) by in-situ XAS and electrochemical assessment. The effect of potential cycling of these mixtures of iridium oxide and elemental metal has been explored to gain insight into whether the iridium oxide emerging from any elemental metal phase may be described as simply AIROF, and to which extent electrochemical post-synthesis treatment results in further oxidation of the elemental metal phase. We thus show — contrary to expectations — that an elemental metal phase persists in the samples even after extensive cycling and that complete conversion into an oxide upon electrochemical post-treatment cannot be expected. In addition, therefore, we will disclose details of the atomic arrangement of the resulting composite elemental iridium metal-AIROF-iridium oxide (PPS) system.

2 Experimental

2.1 Synthesis

An iridium powder was produced by polymeric precursor synthesis, the details are described in by Reksten *et al.* [32]. Two different synthesis series were investigated, which we will refer to as the A- and B-synthesis. For both, a gel was produced by reacting citric acid (CA, Merck 99%) with ethylene glycol (EG, VWR AnalaR Normapur analytical reagent) at 60 °C for 45 minutes while being stirred, after which the temperature was raised to 75 °C, and $H_2IrCl_6 \cdot 4\,H_2O$ (Alfa Aesar 99%) was dissolved in the gel. The ratio between CA, EG and metal was 3:14:1. For the A-synthesis the gel was further heat-treated in air in a quartz crucible partly covered with a lid with a temperature program containing three stages, viz. 30 min at 130 °C, 20 min at 250 °C, and finally 20 min at 500 °C. The temperature was ramped from one temperature to the next at 1 °C min^{-1}. The powder was ground manually with a mortar and pestle after heat treatment. The B-synthesis differed from the A-synthesis by a step consisting of removal of the gel from the furnace after the heat treatment at 250 °C, heat treatment under synthetic air flow and removal of the crucible lid. Crust that had formed during the first two stages was crushed before the sample was re-inserted directly into the furnace and the heat treatment continued as for the A-synthesis by ramping at 1 °C min^{-1} to the final heat treatment for 20 min at 500 °C.

2.2 X-ray powder diffraction and transmission electron microscopy

X-ray powder diffraction (XRD) was performed with Bruker AXS D8Focus using Cu K-α radiation. A zero background silicon sample holder was used. Rietveld analysis was carried out using Bruker AXS TOPAS version 4.2, using a pseudo-Voigt function. The background intensity was accounted for using a Chebychev polynomial of the order 6 to account for the curvature. Refinement of the diffraction pattern was performed within space groups 136 (P42/mnm) and 225 (Fm-3m), in order to obtain the unit cell values, the crystallite size, and fraction of elemental metal and oxide phases. As a figure of merit for the analysis we used [41] $R_{\mathrm{wp}} = \sqrt{\sum_i w_i \left(Y_i^{exp} - Y_i^{th}\right)^2 / \sum_i w_i \left(Y_i^{exp}\right)^2}$, in which Y_i^{exp} is an experimental datum and Y_i^{th} the corresponding theoretical value. The weight factors are defined as $w_i = 1/\left[\sigma\left(Y_i^{exp}\right)\right]^2$ in which $\sigma\left(Y_i^{exp}\right)$ is the standard deviation in Y_i^{exp}.

For imaging by transmission electron microscopy (TEM) the catalyst powder was dispersed in isopropanol in an ultrasonic bath, then dripped onto a copper TEM grid covered with holey carbon film. TEM imaging was performed on a JEOL JEM-2100F.

2.3 Electrochemical Characterization

Electrochemical characterization was performed using a three-electrode electrochemical cell with an aqueous electrolyte containing 0.5 mol dm^{-3} H_2SO_4 (Merck suprapure 96%). All electrolyte solutions were prepared with deionized water (Millipore Direct-Q3 of 18.2 MΩ cm). The reference electrode used was a reversible hydrogen electrode (RHE) in the same electrolyte (0.5 mol dm^{-3} H_2SO_4), and all potentials are referred to this ref-

Physical Chemistry Chemical Physics Accepted Manuscript

This journal is © The Royal Society of Chemistry [year]

View Article Online
DOI: 10.1039/D0CP00217H

Published on 30 March 2020. Downloaded by University of Southampton on 3/31/2020 1:02:17 PM.

Physical Chemistry Chemical Physics Accepted Manuscript

erence electrode. The reference electrode was placed in a separate glass tube with a glass slip bottom where an electrolyte film served as the contact medium between the reference electrode and the electrolyte. This was placed in the same height and $\sim$ 1.5 cm away from the working electrode. A platinum foil was used as the counter electrode and was placed so that it faced the working electrode from the bottom. A Biologic VMP3 potentiostat was used for all the electrochemical measurements. The electrodes characterized in this cell were prepared by the thin film technique[42]. An ink was prepared by dissolving the powder in water (1 mg mL^{-1}) with an ultrasonic bath. 20 µL of the ink was pipetted onto a glassy carbon (GC) RDE with diameter 5 mm (Pine). The ink was dried under a gas stream of N_2. Prior to the ink coating, the GC disc was polished to a mirror finish starting with 5 µm and ending with 0.05 µm alumina paste before being thoroughly rinsed in deionized water and ethanol.

Potential cycling was carried out by cycling the electrode 150 cycles between potential 0 V and 1.5 V with sweep rate of 150 mV s^{-1}. The effect of varying the lower potential boundary and drying the electrode after potential cycling was also explored.

2.4 In situ X-ray Absorption Spectroscopy Electrochemistry

The XAS characterization was carried out in an in situ electrochemical XAS cell in 0.5 mol dm^{-3} H_2SO_4. The cell setup is shown in the Electronic Supplementary Information. The counter electrode of this cell was a ring of Pt mesh and the reference electrode was a mercury mercurous sulfate (MMS) Hg/Hg_2SO_4 placed in a separate tube connected to the cell by a Luggin capillary placed next to the working electrode. The reference electrode was measured to be 704 mV vs. RHE. The working electrode used in this cell was carbon paper painted with a catalyst ink consisting of 20 mg catalyst, 1 mL deionized water, 200 µL isopropanol (AnalaR Normapure VWR), 228 µL 5wt% Nafion® (Alfa Aesar) and 4 mg carbon black (Vulcan XC72R). The ink was sonicated for 1 h before painted onto 0.26 mm thick Toray carbon paper (TGPH-090) until a loading of 0.22 mg cm^{-2}. The sample was then pressed at 130 °C and $\sim$ 1 kg cm^{-2} for 3 minutes. A disk 1.26 cm in diameter was punched out and then hydrated by boiling in deionized water for 20 minutes prior to use. The electrode was cycled in the potential range 0 V through 1.5 V vs RHE 150 cycles at a sweep rate 150 mV s^{-1}. Cycling was paused at n= 0, 25, 100 and 150 for recording of XAS spectra. The potential cycling was started at the open-circuit potential (OCP) and ended at 0.7 V vs. RHE. All XAS spectra were recorded at OCP. The cell was controlled by an Eco Chemie Autolab PGStat30.

2.5 X-ray Absorption Spectroscopy

2.5.1 Data Collection.

The XAS data were collected at the B18-Core XAS beamline of the Diamond Light Source Synchrotron in fluorescence mode using a germanium 9-element detector. The samples were placed at an angle of 45° to the beam and the detector. The ion chamber before the sample was filled with an appropriate mix of inert gases to optimize sensitivity. Data were collected during a multi-bunch electron filling mode of Diamond storage ring providing a maximum current of 300 mA. The data were obtained at the Ir L_{III} edge with a step size of 0.35 eV in the energy range 11015 eV through 12414 eV with a counting time of 60 ms at each step, using a Si(111) double crystal monochromator and Cr-coated collimating and toroidal focusing mirrors. Several scans were collected and summed in order to improve the statistics.

2.5.2 Data reduction.

The XAS data were binned, summed and normalized using Athena, a program in the IFEFFIT package[43]. The absorption edge was measured as the first inflection point in the derivative spectra. The XANES and EXAFS spectra were normalized from 17 eV to 90 eV below the edge and 150 eV to 1090 eV above the edge, respectively. The spectra were carefully deglitched and truncated at the end of EXAFS spectra when needed. The linear combination fit (LCF) procedure in the Athena program was used to fit the XANES spectra to the reference materials which were powders of IrO_2 (Aldrich, 99.9 %), $IrCl_3$ (Alfa Aesar, 99.8 %) and Ir black (Alfa Aesar 99.9 %).

It is desirable to use reference samples which have the same local environment as the sample, only differing in the oxidation state of the element of interest. $IrCl_3$ was employed *in lieu* of such a sample, as has been done in several previous investigations of the oxidation state of Ir in AIROF, EIROF and SIROF[13,14,28].

The LCF was performed of the XANES spectra over a range from 17 eV below the edge to 70 eV above the edge, always applying the normalization range as described above. The energy shifts of the reference spectra were also fitted, but closely monitored and they were always less than 1.1 eV. The fit parameter for the LCF was reported for each fit, defined in Eq. (1),

$$R = \frac{\sum_i^N (|\chi_i^{exp}(k) - \chi_i^{calc}(k)|)^2}{\sum_i^N |\chi_i^{exp}(k)|^2} \quad (1)$$

where $\chi_i^{exp}(k)$ and $\chi_i^{calc}(k)$ are the experimental and theoretical EXFAS fine-structure functions. We will refer to R in Eq. (1) as the "R-factor" to distinguish it from bond lengths.

2.5.3 EXAFS Least-Squares Refinements.

EXAFS least-square refinements were carried out using DL-EXCURV, which performs curve fitting of the theoretical $\chi^{th}(k)$ to the experimental $\chi^{exp}(k)$ using curved wave theory[44]. The calculation of ab inito phase shifts for the expecting neighboring elements also took place in DL-EXCURV. The least-squares refinements were carried out in the wavenumber k range 2 eV through 18 eV, using a k^3 weighting scheme.

The energy shift, E_F, coordination number, N, bond lengths, R, and Debye-Waller factors (DWFs) were refined for six shells. These included shells in both IrO_2 and elemental Ir and are designated as in the third column of Table 1. The table also gives the reference coordination numbers and bond lengths for the corresponding bulk phases. For IrO_2 one of the oxygen shells is located at 1.94 Å and another at 2.00 Å. These two shells were fitted as one single oxygen shell containing six oxygen atoms and thus have the same designation (Ir-O). Refinement of the coordination numbers (N) first and then the other parameters (the energy shift, E_F, bond lengths, R, and Debye-Waller Factors, DWFs) refined si-

View Article Online
DOI: 10.1039/D0CP00217H

Published on 30 March 2020. Downloaded by University of Southampton on 3/31/2020 1:02:17 PM.

multaneously, were repeated until convergence was obtained[32]. Coordination numbers and Debye-Waller factors were decoupled by verifying best fit for both k^2 and k^3 weighting schemes. In addition, coordination numbers were moved manually during refinements of bond lengths and Debye-Waller factors for the given shell, and subsequently refining the shell coordination number, the bond length, and the Debye-Waller factor until convergence. The oxidation state of iridium was inferred from the white line in the XAS spectra and from the coordination numbers of the oxide shells and elemental iridium metal shells, respectively.

Table 1 Coordination number (*N*) and bond lengths (*R*) for iridium oxide and elemental iridium metal

	Shell	Bond	N	Bond length
IrO_2 [45]	1	Ir-O	2	1.94
	2	Ir-O	4	2.00
	3	Ir-Ir,Ox1	2	3.15
	4	Ir-Ir,Ox2	8	3.55
Ir[†]	1	Ir-Ir,Met1	12	2.71
	2	Ir-Ir,Met2	6	3.84
	3	Ir-Ir,Met3	24	4.70

[†] Generated in Atoms (IFEFFIT package[43]) based on ICDD 00-006-0598.

3 Results

3.1 TEM imaging

High-resolution TEM images (see Figs. S.5 and S.6 in the Electronic Supplementary Information (ESI)) to a large degree showed dense areas with little or no contrast. Some areas displayed visible lattice fringes a distance approximately 3.3 Å apart (see Fig. S.6 in the ESI). However, much of the samples were not easily analysed in terms of structure due to the agglomerated nature of these samples, which prevented a thorough structural analysis based on TEM.

3.2 X-ray diffraction

The powder produced by polymeric precursor synthesis A was a mixture of elemental metal and oxide phase, indicated by XRD and quantitative Rietveld refinement of the spectra (Fig. 1). The phase composition was found to be 44.1 wt.% oxide and 55.9 wt.% elemental metal. A similar analysis for the sample made by synthesis B gave a substantially smaller elemental metal fraction, viz. 4.52 wt.%. A synopsis of the structural parameters is given in Table 2. The size of the crystallites for the oxide phase are approximately one fourth of that for iridium oxide synthesized by the hydrolysis synthesis[27].

3.3 Electrochemical Characterization

Cyclic voltammograms for the potential cycling in the potential range 0 V and 1.5 V for a thin film of the catalyst powder prepared by synthesis A and deposited on a glassy carbon (GC) disk are shown in Fig. 2(a). The first and final CV are shown in Fig. 2(b). A symmetrical pair of anodic and cathodic peaks corresponding to the Ir(+3)/Ir(+4) redox couple appear at 0.97 V. These peaks grow continuously during the cycling, but at a decreasing rate. A small anodic prepeak at 0.75 V and a smaller wave close to 1.2 V

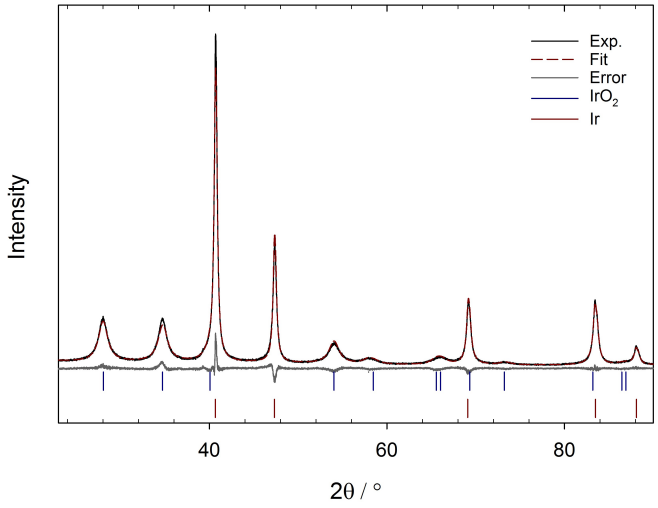

Fig. 1 X-ray diffractogram and Rietveld refinement fit of an iridium sample prepared by synthesis A. R_{wp}=6.30.

are also observed to develop and grow over the course of cycling. The evolution of an anodic peak at $\sim$ 1.45 V which increases the first 30 cycles and then gradually is reduced in size is also apparent. A gradual increase of the anodic charge is seen until approximately the 60th cycle at which it becomes stable, Fig. 2(c).

A set of peaks possibly due to adsorption and desorption of hydrogen is seen for the first cycle at potentials below approximately 0.4 V in Figures 2(a) and 2(b). Several distinct desorption peaks are often seen for bare elemental Ir metal in the potential range 0.06 V through 0.4 V[46,47]. The waves in this potential region are not as distinct as those found in the in the literature for elemental iridium metal[46,47], and are somewhat rounder in shape. They do, however, have the same appearance as the hydrogen desorption peaks that appear after hydrous oxide growth on Ir[47]. Still, two small distinct peaks are well resolved in the initial voltammograms in Figures 2(a) and 2(b) at potentials corresponding to hydrogen desorption peaks at elemental iridium metal. These features in the initial cyclic voltammograms in Figures 2(a) and 2(b) in this potential region are therefore to some degree consistent both with elemental iridium metal and iridium oxide, and possibly represent a superposition of both in the surface.

The features in the voltammograms below approximately 0.4 V in Fig. 2 disappear completely upon cycling the electrode potential.

Assuming the peaks in the potential region below 0.4 V to be due to hydrogen desorption and adsorption we may estimate the surface area of the elemental metal part of the sample from integrating the difference between the anodic currents for the first and final cycle of Fig. 2(b). This gives a charge of approximately 90 μC. Assuming a charge density for hydrogen underpotential-deposition (H-UPD) of[48] 0.21 mC cm^{-2} this corresponds to approximately 0.4 cm^2, and with a loading of 20 μg at the electrode (see Experimental) of which approximately half is elemental iridium metal this gives a specific surface area in the order of 4 m^2 g^{-1} of catalyst (oxide and elemental iridium metal). If we assume each crystallite to be freely exposed to the solution we obtain

Physical Chemistry Chemical Physics Accepted Manuscript

This journal is © The Royal Society of Chemistry [year]

View Article Online
DOI: 10.1039/D0CP00217H

Published on 30 March 2020. Downloaded by University of Southampton on 3/31/2020 1:02:17 PM.

Table 2 The unit cell lengths a and c, crystallite size d, and weight fractions of IrO_2 and Ir obtained from Rietveld analysis of samples made by the A and B synthesis procedure

	IrO_2				Ir			
Synthesis	a / Å	c / Å	d / nm	wt.%	a / Å	d /nm	wt.%	R-factor
A	4.5051(3)	3.1521(4)	4.73(3)	44.1(1)	3.84023(7)	16.91(5)	55.9(1)	6.31
B	4.5156(5)	3.1518(4)	3.47(2)	95.48(6)	3.8368(3)	17.4(4)	4.52(6)	6.77

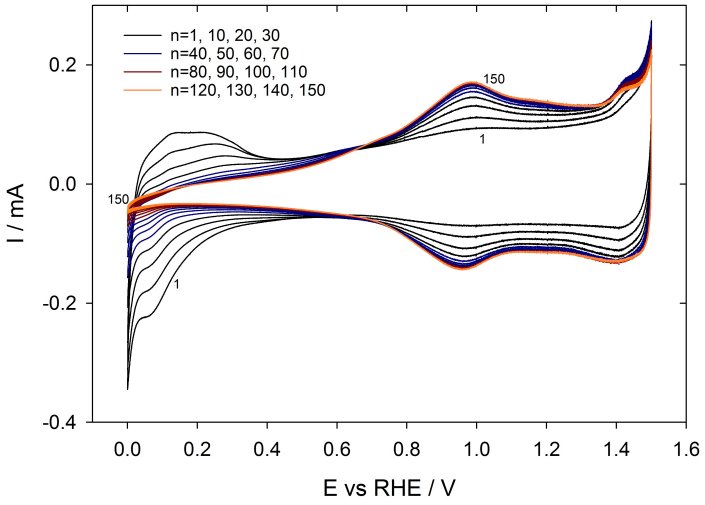

(a) CV as a function of cycle number

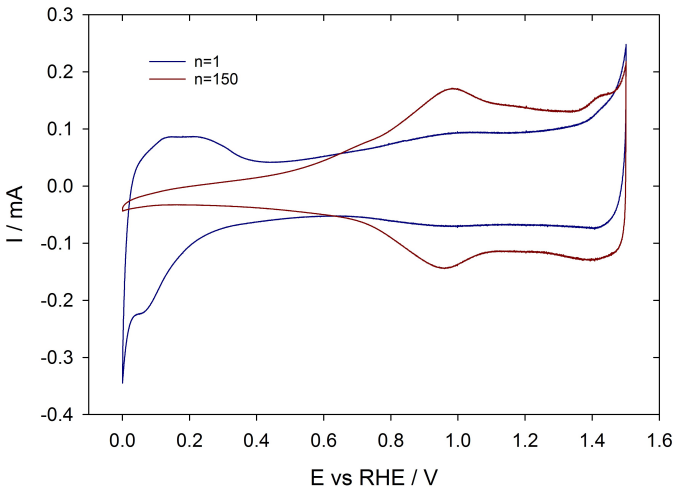

(b) First and final cycle

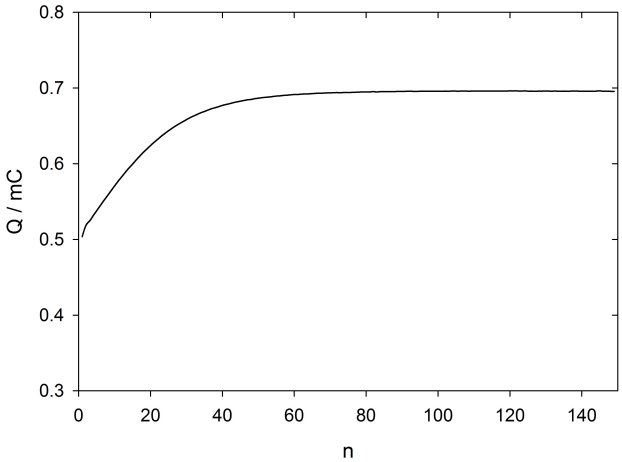

(c) Charge as a function of cycle number

Fig. 2 (a) Evolution of cyclic voltammogram as function of potential cycling for the first and every tenth cycle, (b) the first and final cycle, (c) the charge as function of cycling. Characterization of IrO_2/Ir thin film on glassy carbon with sweep rate $150\ \mathrm{mV\ s^{-1}}$, $0.5\ \mathrm{mol\ dm^{-3}}$ H_2SO_4 electrolyte. The sample was prepared by synthesis A.

Physical Chemistry Chemical Physics Accepted Manuscript

View Article Online
DOI: 10.1039/D0CP00217H

Published on 30 March 2020. Downloaded by University of Southampton on 3/31/2020 1:02:17 PM.

approximately 10 m^2 g^{-1} from simple geometric considerations. While these estimates are rather rough, they appear to indicate that a very large fraction of the crystallites are exposed to the electrolyte.

Changing the lower vertex potential for the cycling from 0 V to 0.2 V resulted in voltammograms that did not change from cycle to cycle as shown in Fig. 3. In particular, there were no signs of any growth of oxide peaks such as those in the voltammograms with the lower limit set to 0 V (Fig. 2(a)). However, setting the lower potential limit to 0 V and performing another 150 cycles for *the same sample* did again result in voltammograms similar to those obtained with the lower potential limit set to 0 V in the first place. As before the charge increased from cycle to cycle and with peaks developing as in Fig. 2(a). In order for the oxidation process to occur and result in growing oxide peaks it is therefore necessary that the lower vertex potential (E_1) is lower than 0.2 V.

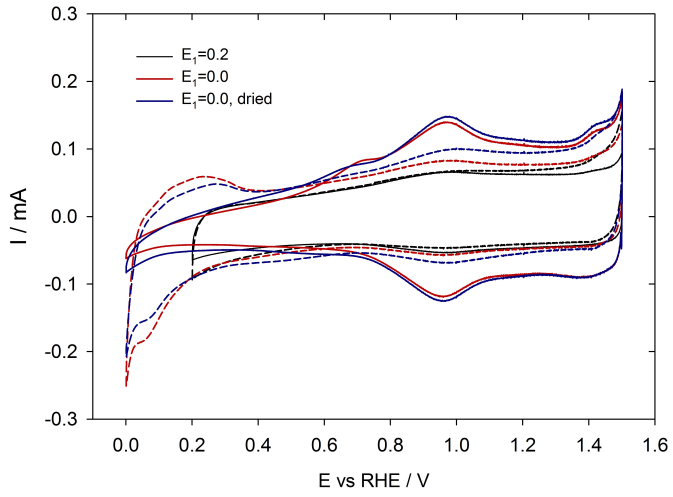

Fig. 3 Evolution of the cyclic voltammograms upon of potential cycling at cycle *n*=1 and 150 with lower potential boundary, E_1, equal 0.2 V (black) and E_1=0.0 V (red). First cycles are shown with dashed lines, cycles *n*=150 are shown with solid lines. The film was dried after final cycle with E_1=0.0 V, and cycle *n*=1 and 150 shows evolution after drying (blue). Characterization of IrO_2/Ir thin film on glassy carbon with sweep rate 150 mV s^{-1}, 0.5 mol dm^{-3} H_2SO_4 electrolyte. The sample was prepared by synthesis A.

Further drying of the same electrode under a N_2 gas flow for eight hours caused the subsequent voltammograms to change back to the shape characteristic of original, pristine films to a substantial degree. Comparing the first cycle recorded before the electrode was dried (with lower vertex potential equal to 0.0 V) to the first cycle after drying reappearance of hydrogen desorption and adsorption peaks are seen (Fig. 3). The hydrogen adsorption/desorption peaks after drying are smaller than for the initial cycle with E_1 =0.0 V, and a reduction of the charge associated with the Ir(+3)/Ir(+4) peaks was seen after the electrode had been dried. By drying in a nitrogen atmosphere the iridium structure has therefore almost been returned to the state it had before potential cycling, although not completely. Upon potential cycling after drying, the electrode growth of Ir(+3)/Ir(+4) peaks are again observed, this time with charge slightly surpassing what was obtained during the previous cycling; After drying it took only 25 cycles to reach the same voltammetric charge as reached after 150 cycles prior to drying. The appearance of the Ir(+3)/Ir(+4) peaks and the disappearance of the peaks in the potential region below 0.4 V always occurred in concert, and both were almost reversible with drying of the electrode.

Cyclic voltammograms for the potential cycling in the potential range 0 V and 1.4 V for a thin film of the catalyst powder prepared by synthesis B and deposited on a glassy carbon (GC) disk are shown in Fig. 4. The voltammograms for the samples prepared by synthesis B did not change appreciably with cycle number and no developing peaks such as those in Fig. 2 were apparent. Both voltammograms in Fig. 4 are similar to previous results on IrO_2 prepared by the hydrolysis method [15,32] and by the Pechini method [18,39] above 0.4 V. However, the voltammogram for the first cycle of the powder from the A-synthesis has relatively pronounced peaks in the potentials below 0.4 V compared to those in the references [15,18,32,39].

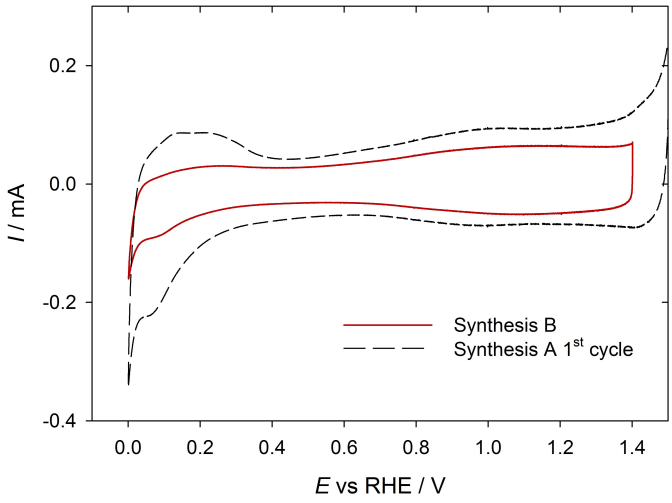

Fig. 4 Cyclic voltammogram (red solid line) for an IrO_2 sample on glassy carbon with sweep rate 20 mV s^{-1} in 0.5 mol dm^{-3} H_2SO_4 electrolyte. The sample was prepared by synthesis B. The first cyclic voltammogram from Fig. 2 is shown for comparison (dashed line).

3.4 Linear Combination Fitting of in-situ XANES

The evolution of cyclic voltammograms for the sample prepared by the A-synthesis as function of cycle number in the in-situ XAS-cell is show in Fig. 5. The voltammograms thus evolved in a very similar way and display the same features as in the those for the catalysts as thin films on glassy carbon in Figures 2(a) and 2(b) above. (The potential cycling was paused after 25, 100, and 150 cycles for recording of the X-ray absorption spectra.)

The XANES spectra of the Ir, IrO_2 and $IrCl_3$ reference samples are shown in Fig. 6. The XANES spectra of the PPS iridium oxide sample prepared by synthesis A recorded as the cycling was paused after *n* potential cycles are shown in Fig. 7. Only minor

Physical Chemistry Chemical Physics Accepted Manuscript

This journal is © The Royal Society of Chemistry [year]

View Article Online
DOI: 10.1039/D0CP00217H

Published on 30 March 2020. Downloaded by University of Southampton on 3/31/2020 1:02:17 PM.

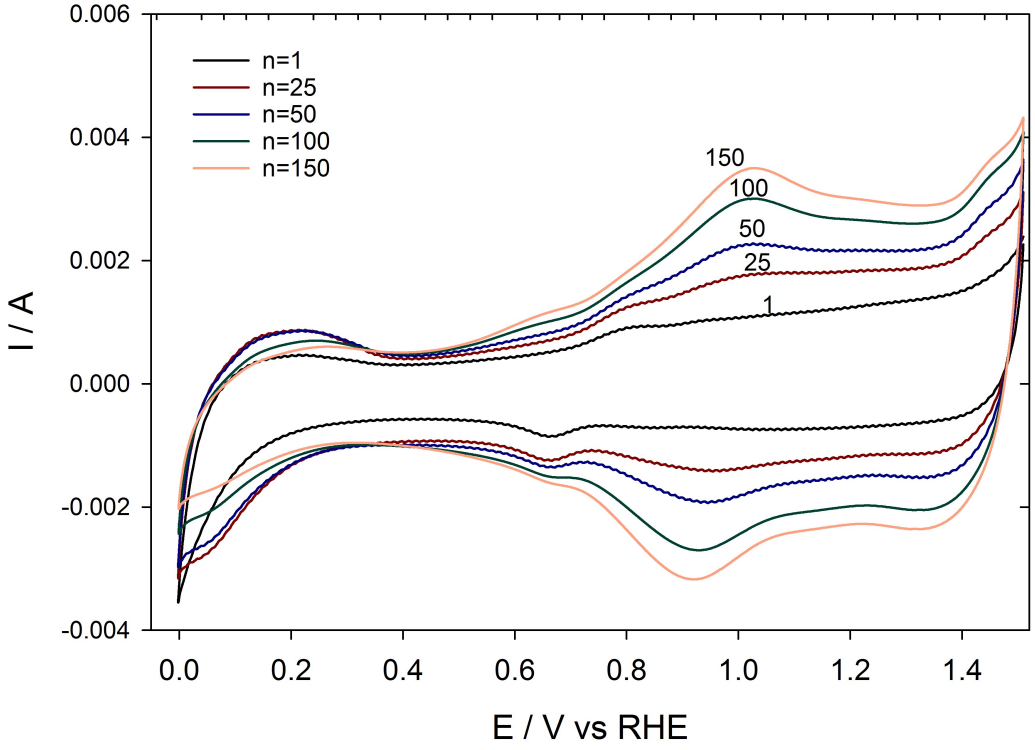

Fig. 5 Evolution of the cyclic voltammograms for a sample prepared by the A-synthesis as function of potential cycling in the in situ XAS cell, *n*=1, 25, 50, 100 and 150. Characterization of IrO_2/Ir painted onto carbon paper with sweep rate $150\ \mathrm{mV\ s^{-1}}$, $0.5\ \mathrm{mol\ dm^{-3}}$ H_2SO_4 electrolyte.

Physical Chemistry Chemical Physics Accepted Manuscript

View Article Online
DOI: 10.1039/D0CP00217H

Published on 30 March 2020. Downloaded by University of Southampton on 3/31/2020 1:02:17 PM.

changes can be observed in these XANES spectra over the course of potential cycling. The only exception is a small increase of the white line as function of n. The difference plot, the inset in Fig. 7(a), demonstrates this small increase of the white line in which the spectrum for n=0 has been used as the standard. The first derivative of the spectra is shown in Fig. 7(b). A small shift in the peak position from lower to higher energy is seen as function of cycling in Fig. 7(b), as one would expect with increased oxidation from the reference spectra in Fig. 6(b). However, the shift is very small and indicates only a small degree of oxidation upon potential cycling.

Fig. 8 shows an example of the linear combination fit of the spectra recorded before cycling, n=0, with and without Ir^{+3} in the fit, Fig. 8(a) and 8(b), respectively. The inclusion of Ir(+3) in the model does not appear to be critical to the fit.

The results obtained from LCF for the sample prepared by the A-synthesis are given in Table 3 and 4, where the elemental metal fractions, energy shifts and R-factors obtained ex situ and as function of potential cycling in situ have been summarized for the fits with Ir^{+3} excluded and included, respectively. From the results in Table 3 a decrease of 4.7 at.% is seen for the elemental metal fraction over the course of potential cycling. If Ir^{+3} is included in the fit, the reduction of the fraction of elemental iridium metal is a mere 1 at.% and the fraction of Ir^{+3} is reduced from from 7 to 2 at.%. (As expected, slightly better R-factors were obtained when all three references were included in the LCF.) Any presence of Ir^{+3} might be due to incomplete decomposition of $IrCl_3$ or formation of intermediate Ir_2O_3 [49,50]. From theoretical considerations Ir_2O_3 is expected to be unstable[51] unless the chemical potential of oxygen is very low. However, the decrease in the elemental metal fraction upon cycling is very small independent of whether Ir(+3) is included in the fit or not, and demonstrates that any significant oxidation of the elemental metal phase did not occur over the course of potential cycling.

Table 3 The atomic fractions of Ir^0, the energy shifts, E_F and R-factors obtained in the LCF of the XANES spectra for the sample prepared by the A-synthesis. In this series the Ir^{+3} standard was excluded from the LCF

	At. fraction Ir^0	E_F, Ir^0 /eV	E_F, Ir^{+4}	R-factor
ex situ	0.767(2)	-0.14(1)	1.04(2)	4.22×10^{-4}
n=0	0.762(2)	0.10(1)	0.90(2)	3.39×10^{-4}
n=25	0.750(2)	0.15(1)	0.78(2)	2.83×10^{-4}
n=100	0.735(2)	0.11(1)	0.78(2)	2.71×10^{-4}
n=150	0.720(2)	0.19(1)	0.79(2)	3.67×10^{-4}

3.5 EXAFS Least-Squares Refinement

Fig. 9(a) shows experimental EXAFS data for $k^3\chi(k)$ plotted vs. wavenumber k. The data were recorded ex situ and in situ before cycling. A corresponding comparison between $k^3\chi(k)$ prior to cycling and after 150 cycles is shown in Fig. 9(b). The corresponding comparisons of the Fourier transforms are shown in Figures 9(c) and 9(d). For both types of plot the ex situ data are rather similar to those recorded in situ prior to cycling. However, upon cycling some slight changes appear at high k in the plot of $k^3\chi(k)$ and more noticeably in the 3 Å – 4 Å range in the Fourier transform, Fig. 9(a), i.e. in the range of the third and fourth shells of IrO_2 (Ir-Ir,Ox1 and Ir-Ir,Ox2) and first and second of elemental Ir (Ir-Ir,Met1 and Ir-Ir,Met2), Table 1.

Fig. 10 shows the EXAFS Fourier transforms and k^3 μ(k) for both ex situ and in situ spectra as a function of cycling for the sample prepared by the A-synthesis. An overview of the fitting parameters is given in the ESI. As expected from the LCF of XANES no significant differences can be observed between the spectra in Fig. 10.

The bond lengths, Debye-Waller factors and the coordination numbers obtained from EXAFS for the sample prepared by the A-synthesis prior to cycling (in situ, $n = 0$) are given in Table 5. The table also includes corrected multiplicities $N_{\mathrm{corr}} = N_{\mathrm{exp}}/f$, in which N_{exp} is the experimentally obtained coordination number (from EXAFS) and f the fraction of the corresponding phase in the sample (from LCF of XANES). This way of correcting the coordination numbers was suggested by Martens et al.[32,52] and gives estimates of what the coordination numbers would have been if either the oxide or elemental metal phase, respectively, was the sole phase present.

We thus assume that if the iridium-oxygen coordination numbers in our samples are lower than those expected for bulk IrO_2 then this implies that the relative fraction of iridium oxide in the sample is lower than one. This follows from the fact that EXAFS is a method that averages over the entire sample. Thus, if only a fraction f = f_{ox} of the iridium atoms belongs to the oxide phase (IrO_2), then only this fraction f_{ox} of the total of iridium atoms in the sample will have oxygen atoms as neighbours (in the distances given in Table 1). Therefore, the experimental coordination number for each of the shells for IrO_2 in Table 1 are expected to be equal to the coordination number for that shell in bulk IrO_2 (N in Table 1) multiplied by f_{ox}. (The iridium atoms in the elemental iridium metal phase will have no such oxygen neighbours. The coordination numbers for the elemental iridium phase will — by a similar argument — be equal to the bulk coordination number multiplied by the factor f = (1 - f_{ox}).) One may write this as $N_{\mathrm{exp}} = fN$, in which N_{exp} is the experimentally obtained coordination number and N corresponding coordination number in bulk (Table 1). We therefore attempt to correct the coordination numbers obtained experimentally for the presence of another phase by division by f, i.e. $N_{\mathrm{corr}} = N_{\mathrm{exp}}/f$ in which N_{corr} is the corrected coordination number and N_{exp} the experimental value.

Table 5 includes the coordination numbers corrected using the phase fractions obtained both from the LCF of XANES excluding and including Ir^{3+} in the fits, respectively. The bond lengths are similar to nominal bond lengths. However, the coordination numbers are only similar to nominal coordination numbers after correcting for the composition, i.e. the corrected multiplicities.

The experimental and corrected multiplicities for the two first IrO_2 shells (both Ir-O) in Table 1 are shown in Fig. 11 as function of the number of cycles. Coordination numbers obtained directly from the EXAFS analysis and the corrected multiplicities are shown. Corrections employing the fractions obtained from LCF of the XANES from fits in which Ir^{+3} were excluded are la-

Physical Chemistry Chemical Physics Accepted Manuscript

This journal is © The Royal Society of Chemistry [year]

View Article Online
DOI: 10.1039/D0CP00217H

Published on 30 March 2020. Downloaded by University of Southampton on 3/31/2020 1:02:17 PM.

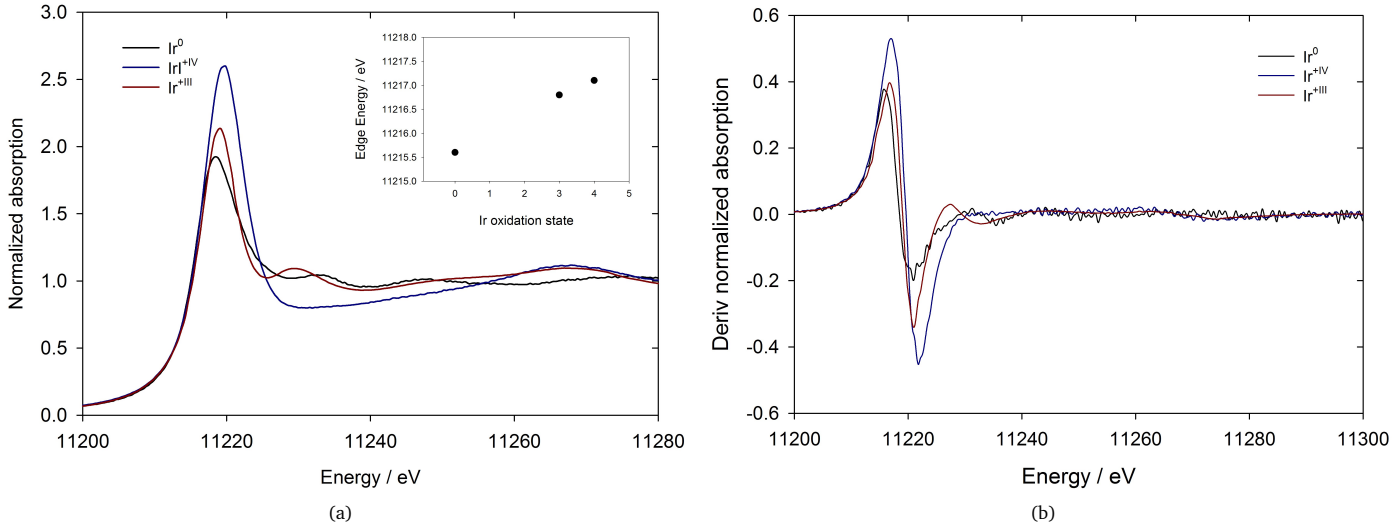

(a) (b)

Fig. 6 XANES spectra at Ir L_{III} edge of the reference samples Ir (Ir^0) (elemental metallic iridium), $IrCl_3$ (Ir^{+3}) and IrO_2 (Ir^{+4}), (a) normalized absorption, inset show graph of edge position versus oxidation state, (b) first derivative of normalized absorption.

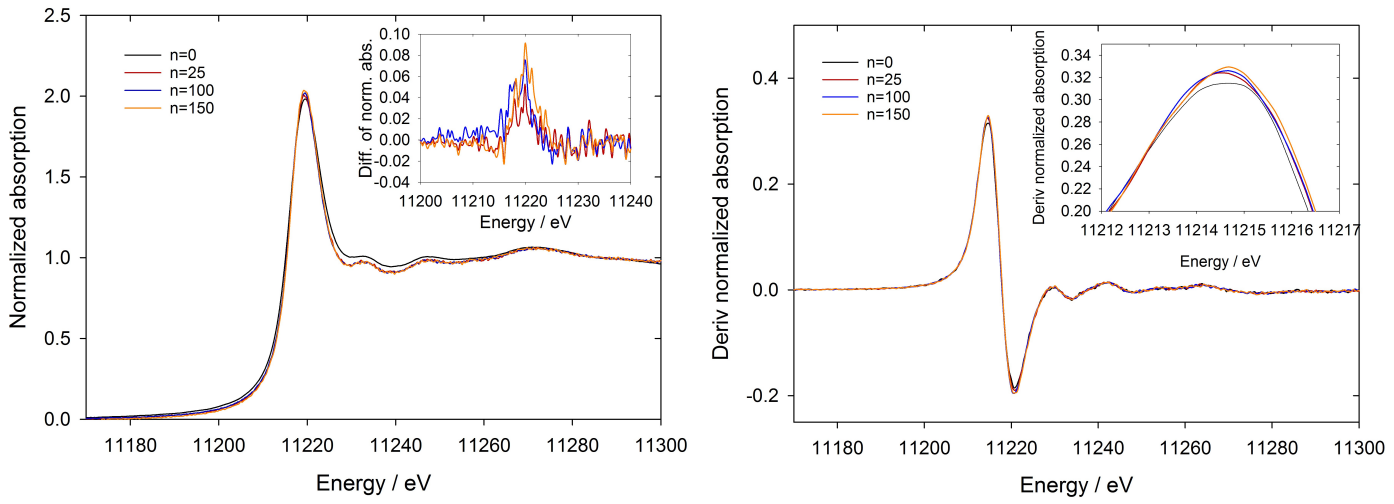

(a) (b)

Fig. 7 XANES spectra for a sample prepared by the A-synthesis after potential cycling *n*=0, 25, 100 and 150, (a) normalized absorption, with difference plot insert where the *n*=0 was the standard used, (b) first derivative of normalized absorption with inset of zoom-in of the first peak.

Table 4 The atomic fractions of Ir^0, Ir^{+3} and Ir^{+4}, the energy shifts, E_F and R-factors obtained in the LCF of the XANES spectra for the sample prepared by the A-synthesis. In this series the Ir^{+3} standard was included in the LCF

	At. fraction Ir^0	E_F, Ir^0	At. fraction Ir^+3	E_F, Ir^+3	At. fraction Ir^+4	E_F, Ir^{+4}	R-factor
ex situ	0.71(3)	-0.23(2)	0.07(1)	1.1(2)	0.22(1)	1.01(4)	3.55×10^{-4}
n=0	0.71(2)	0.06(2)	0.05(1)	0.7(3)	0.24(2)	1.12(3)	3.11×10^{-4}
n=25	0.71(2)	0.15(2)	0.04(1)	0.2(3)	0.25(1)	0.96(2)	2.67×10^{-4}
n=100	0.696(9)	0.06(2)	0.04(1)	0.8(3)	0.26(1)	0.83(3)	2.53×10^{-4}
n=150	0.70(1)	0.17(2)	0.02(1)	1.0(7)	0.28(2)	0.81(3)	3.61×10^{-4}

Physical Chemistry Chemical Physics Accepted Manuscript

View Article Online
DOI: 10.1039/D0CP00217H

Published on 30 March 2020. Downloaded by University of Southampton on 3/31/2020 1:02:17 PM.

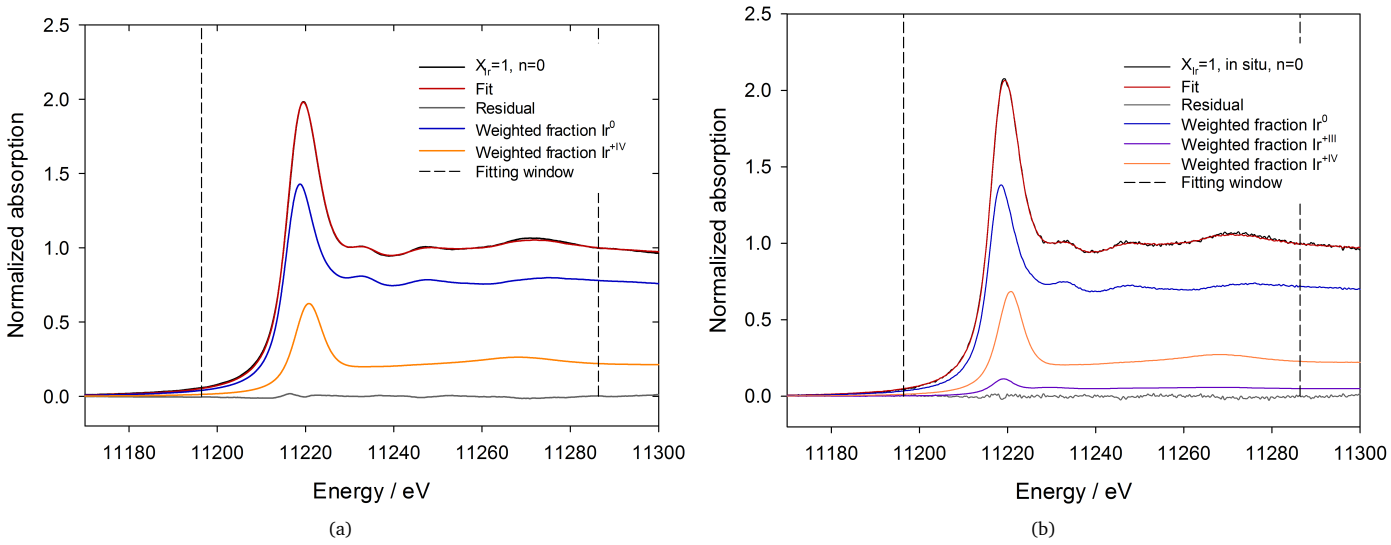

Fig. 8 Example of the LCF for a sample prepared by the A-synthesis, n=0, normalized μ(E), (a) with reference spectra of Ir^0 and Ir^{+4} (R-factor 3.39×10^{-4}), and (b) Ir^0, Ir^{+3} and Ir^{+4} (R-factor 3.11×10^{-4}).

belled "Corrected multiplicities 1", and those employing LCF of XANES including Ir^{+3} are labelled "Corrected multiplicities 2". The coordination number does not change beyond the estimated errors, which are significant, during the potential cycling. This is to be expected since only a small decrease in the fraction of elemental iridium as a function of the number of cycles is apparent from the LCF of the XANES spectra.

None of the other bond lengths and coordination numbers given in Table 5 changed significantly during potential cycling, although a small decrease in bond length is discernible in the first shell of elemental iridium, $R_{\mathrm{Ir-Ir,Met1}}$, and in that of the third metal oxide shell, $R_{\mathrm{Ir-Ir,Ox2}}$, as the number of cycles increased. The coordination number for the first elemental metal shell, $N_{\mathrm{Ir-Ir,Met1}}$, also displayed a small increase. Figures showing the dependence of all the bond lengths and coordination numbers given in Table 5 are given in the ESI as Figures S.2 and S.3. The ESI also includes figures showing the Debye-Waller factors as a function of cycle number. By and large these showed a similar lack of dependence on the cycle number as the coordination numbers, perhaps with the exception of that for shell 2 for elemental iridium ('Ir-Ir,Met2', Table 1) which showed a small but systematic decrease with increasing cycle number.

In addition to estimating phase composition with respect to elemental iridium metal and iridium by LCF of XANES and Rietveld analysis already presented above, we also estimated the fraction based on the experimentally obtained multiplicity for the oxygen shell (MOS). We do this by turning around the formula used for obtaining corrected multiplicities above to compute the fraction of a given phase as $f = N_{\mathrm{exp}}/N$. (In their EXAFS analysis of rhodium catalysts Martens *et al.* [52] estimated the fraction of oxidized rhodium based on a similar comparison of the experimentally obtained rhodium-oxygen coordination number to that for bulk Rh_2O_3.) We will refer to this procedure as the MOS method.

We therefore computed the oxide fraction for our samples by the MOS method as $f_{\mathrm{ox}} = N_{(\mathrm{Ir-O})\mathrm{exp}}/6$ since we regard the two first shells as one in our analysis. The result for the elemental metal fraction evaluated from the MOS method, quantitative Rietveld analysis of XRD spectra, and LCF of XANES are listed in Table 6. All XAS methods (ex situ) indicate larger fractions of elemental metal than obtained by Rietveld analysis. A reduction in elemental metal fraction is seen for all the XAS methods as function of potential cycling, but within the uncertainties in at. % presented of these methods only the LCF of XANES with two reference spectra included demonstrates any significant reduction in elemental metal fraction, but is also in this case small. All methods therefore indicate that the elemental metal fraction was either unchanged or was reduced slightly.

Table 6 Estimation of fractions elemental iridium metal for the sample prepared by the A-synthesis based on quantitative Rietveld analysis of XRD spectra, LCF of XANES spectra and reduced multiplicity of the oxygen shell (MOS) method. All fractions are reported in at.% Ir^0. In the final column the coordination numbers used to evaluate the phase fractions with the MOS method are listed

	XRD	LCF XANES Ir^{+3} not included	LCF XANES Ir^{+3} included	MOS	$N_{\mathrm{Ir-O,exp}}$
ex.situ	59.5(1)	76.7(2)	71(3)	72(5)	1.7(3)
n=0	-	77.3(2)	71(2)	72(9)	1.7(5)
n=25	-	76.0(2)	71(2)	66(9)	2.1(6)
n=100	-	74.2(2)	69.6(9)	67(9)	2.0(5)
n=150	-	73.8(2)	70(1)	67(9)	2.0(6)

In addition, small particle size may contribute to the coordination numbers being lower than those for the corresponding bulk phase. Of the three elemental metal shells all N_{corr} are less than what expected for the (pure) bulk, which is to be expected for sufficiently small particles [53]. The multiplicity of the Ir-Ir elemental metal shells might therefore indicate the elemental iridium metal

Physical Chemistry Chemical Physics Accepted Manuscript

This journal is © The Royal Society of Chemistry [year]

View Article Online
DOI: 10.1039/D0CP00217H

Published on 30 March 2020. Downloaded by University of Southampton on 3/31/2020 1:02:17 PM.

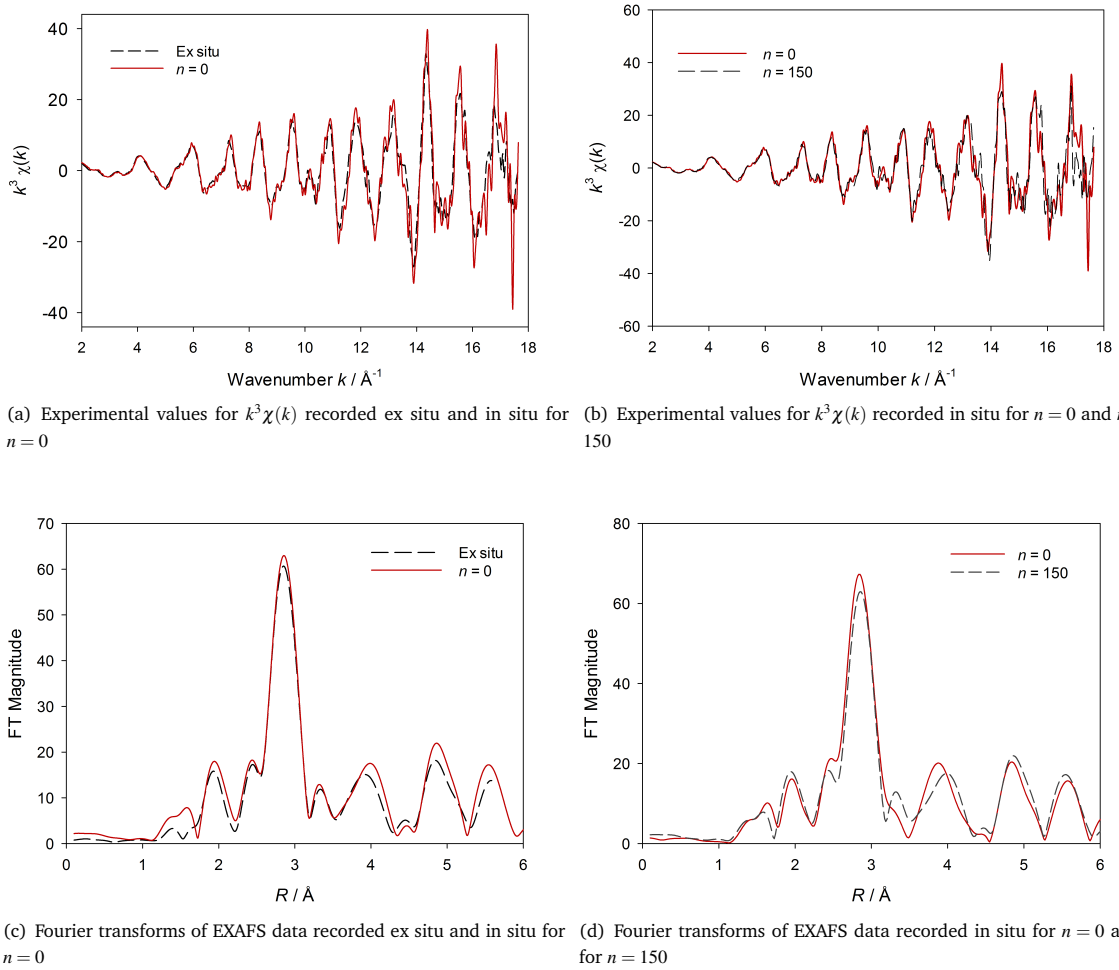

(a) Experimental values for $k^3\chi(k)$ recorded ex situ and in situ for $n = 0$

(b) Experimental values for $k^3\chi(k)$ recorded in situ for $n = 0$ and $n = 150$

(c) Fourier transforms of EXAFS data recorded ex situ and in situ for $n = 0$

(d) Fourier transforms of EXAFS data recorded in situ for $n = 0$ and for $n = 150$

Fig. 9 (a) Comparison of experimental data for $k^3\chi(k)$ recorded ex situ and in situ for $n = 0$. (b) Comparison of experimental data for $k^3\chi(k)$ recorded in situ for $n = 0$ and $n = 150$. (c) Comparison of Fourier transforms of EXAFS data recorded ex situ and in situ for $n = 0$. (d) Comparison of Fourier transforms of EXAFS data recorded in situ for $n = 0$ and for $n = 150$. The sample was prepared by the A-synthesis.

Table 5 Bond lengths, Debye-Waller factors (DW), and coordination numbers (CN) for IrO_2 and Ir measured in situ before cycling ($n = 0$ cycles). The sample was prepared by the A-synthesis. The R-factor was 41.38 and the k-range $2\ \text{Å}^{-1} - 18\ \text{Å}^{-1}$.

	Bond length / Å	DW / Å^2	CN	CN/f (3+ excluded)	CN/f (3+ included)	Nominal CN
Ir-O	1.97(1)	0.003(2)	1.7(3)	7(2)	5(2)	6
Ir-Ir, Met1	2.706(3)	0.0067(2)	6.3(3)	8.2(5)	8.9(6)	12
Ir-Ir, Ox1	3.15(1)	0.003(2)	0.6(2)	3(2)	2(1)	2
Ir-Ir, Ox2	3.534(9)	0.003(1)	1.3(2)	6(2)	5(1)	8
Ir-Ir, Met2	3.831(9)	0.006(1)	3.3(6)	4(1)	5(1)	6
Ir-Ir, Met3	4.708(7)	0.0085(8)	10(1)	13.0(3)	14.1(5)	24

Physical Chemistry Chemical Physics Accepted Manuscript

View Article Online
DOI: 10.1039/D0CP00217H

Published on 30 March 2020. Downloaded by University of Southampton on 3/31/2020 1:02:17 PM.

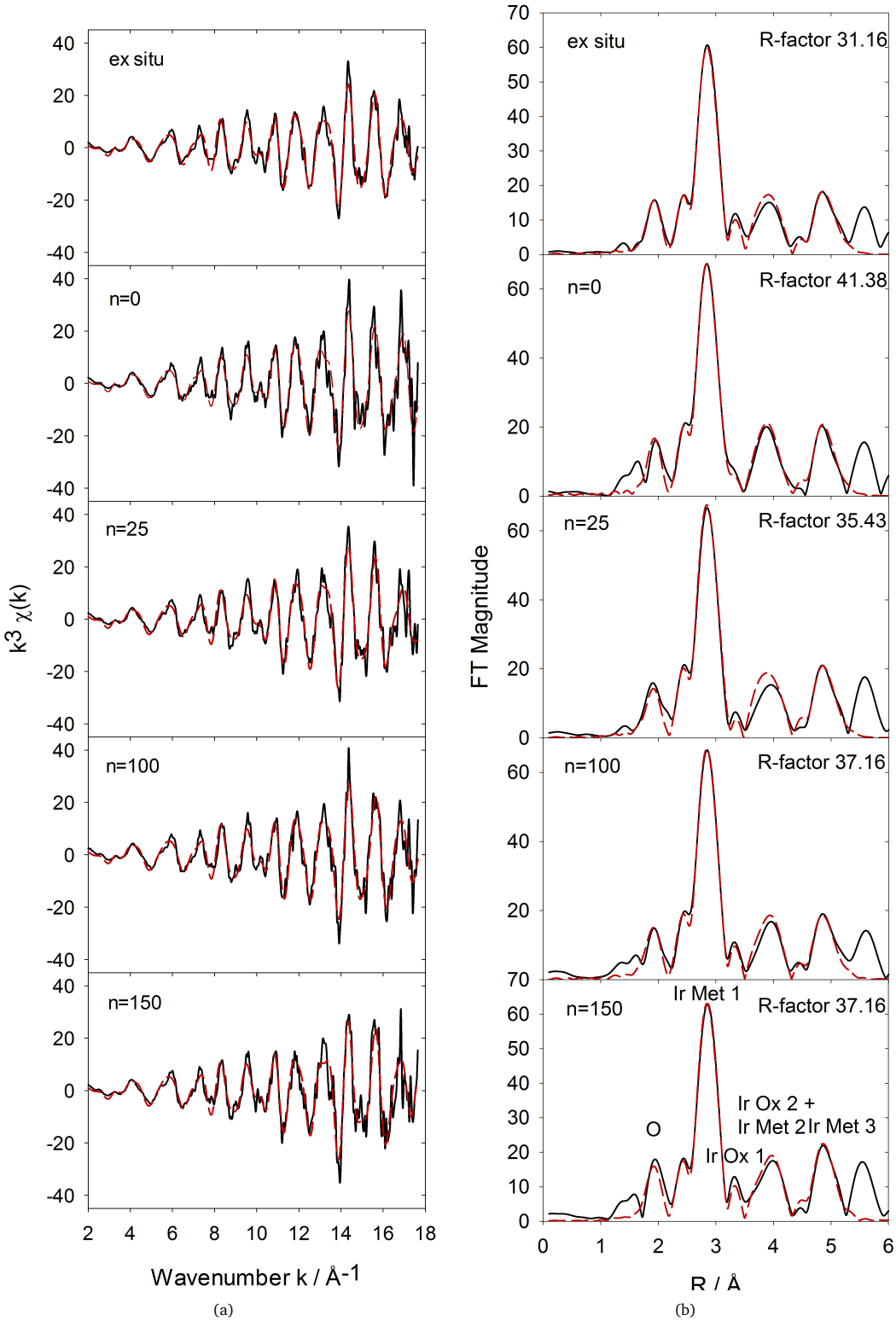

Fig. 10 Experimental (-) and least squares refined (- -) of k^3 χ(k) (a) and EXAFS Fourier transforms (b) obtained ex situ (top), and in situ *n*=0 to *n*=150 (bottom) during potential cycling of the sample prepared by the A-synthesis.

Physical Chemistry Chemical Physics Accepted Manuscript

This journal is © The Royal Society of Chemistry [year]

View Article Online
DOI: 10.1039/D0CP00217H

Published on 30 March 2020. Downloaded by University of Southampton on 3/31/2020 1:02:17 PM.

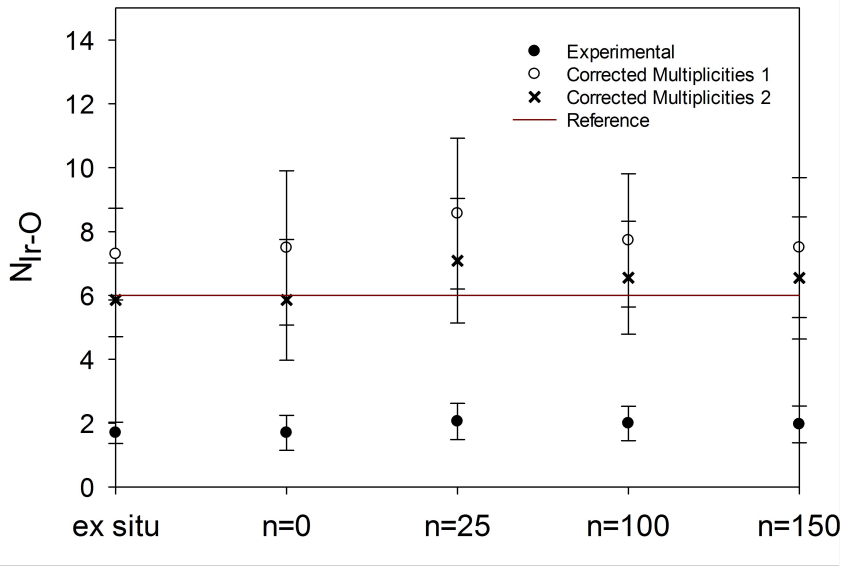

Fig. 11 Experimentally obtained coordination number for the first oxygen shell of IrO_2 (Ir-O) N_{Ir-O} and the same coordination number corrected by reduced fraction (N_{corr}=N_{exp}/f_{ph}) as function of cycle number n. The sample was prepared by the A-synthesis. Corrected multiplicity 1 and 2 are the experimentally obtained N divided by the oxide fraction found without and with Ir^{+3} included in the LCF of XANES, respectively. The reference value for the coordination number is indicated by the red line.

is present in the form of small Ir-particles.

The experimentally obtained bond length for the first (combined) oxygen shell Ir-O for IrO_2 as function of potential cycling of the sample prepared by the A-synthesis is shown in Fig. 12. A reference bond length is not provided as this shell represents a mix of two different bond lengths, one at 1.94 Å with two atoms and one at 2.00 Å with four atoms and since these have been refined as one shell consisting of six oxygen atoms. The bond lengths obtained were more or less stable during the cycling, with some exceptions, Fig. S.3 in the ESI. The first elemental metal shell, Fig. S.3(b), and the second metal oxide shell, Fig. S.3(d), show the largest deviation from the reference values, and both show a contraction over the course of cycling.

4 Discussion

The electrochemical data (Figures 2, 4, and 7) show that the increasing oxide peaks during potential cycling for the sample prepared by the A-synthesis must be limited to the regions of the sample in which iridium is in oxidation state zero (elemental iridium metal). The intercalation of protons related to the Ir(+3)/Ir(+4) process is believed to proceed according to[22,54] Eq. 2

$$IrO_2 \cdot nH_2O + (1+\delta)H^+ + \delta A^- + e^- \rightleftharpoons IrO_{1-\delta}(OH)_{1+\delta}\delta A \cdot mH_2O + (n-m)H_2O \quad (2)$$

corresponding to the peak at 0.97 V in Figures 2 and 4. This part of the voltammogram is similar for both samples. The B-sample is essentially free of any elemental iridium metal, and the voltammograms for this sample were stable in the potential range of Eq. 2. This demonstrates that iridium oxide prepared by PPS with precautions taken so that little or no elemental metal is formed will not change upon cycling as opposed to for example iridium oxide prepared by sputtering[55].

The data for the cycles with $n > 1$ in Fig. 2 may therefore be understood as a superposition of PPS oxide and AIROF. This is supported by the fact that if the part of the current corresponding to the PPS-part of the iridium-iridium oxide composite is subtracted from the voltammogram one is left with a CV that looks essentially like that of AIROF in the potential region of Eq. (2)[12,22,25,56,57].

The XAS data show that the appearance of oxide peaks during potential cycling (Figures 2 and 7) must be due to structural and compositional changes strictly limited to the surface of the regions of the samples prepared by the A-synthesis initially containing elemental iridium. By LCF of the XANES spectra recorded as function of potential cycling the decrease in the fraction of elemental iridium metal in the samples is less than 5 at.%, supported by the absence of any significant changes in the coordination numbers with cycling. To reconcile the absence of any significant increase in elemental metal from the XAS measurements with the results of cyclic voltammetry and the reversible change of the CV with drying, it must be assumed that any oxide layer formed at elemental iridium metal in the sample, is thin.

The fact that the lower vertex potential has to be lower than 0.2 V (Fig. (3)) for the onset of the growth is consistent with the growth mechanism for iridium oxide on elemental iridium metal as proposed by Pickup and Birss[47]. According to these authors oxidation and reduction of the iridium surface involves three layers. A compact inner oxide is initially produced by a place-exchange mechanism as the potential is increased to 1.2 V. At higher potentials up to 1.5 V the surface of the inner oxide will be further

Physical Chemistry Chemical Physics Accepted Manuscript

View Article Online
DOI: 10.1039/D0CP00217H

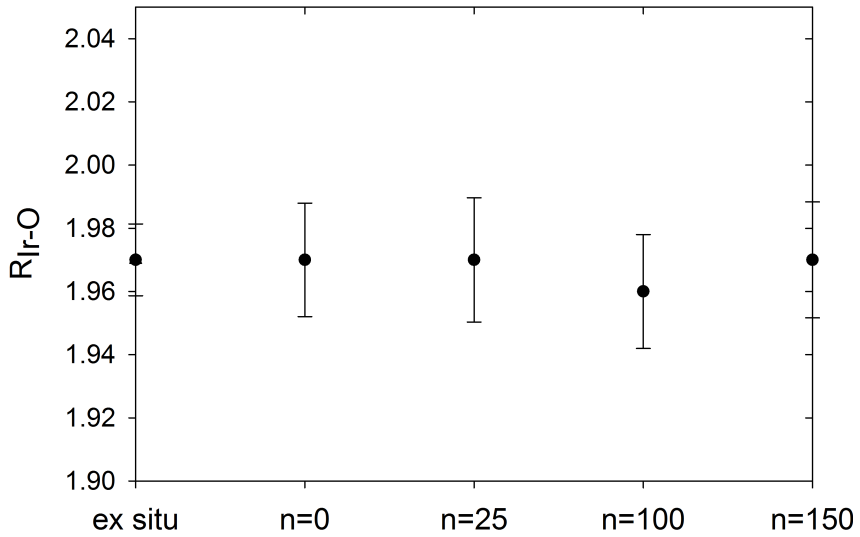

Fig. 12 Experimentally obtained bond lengths R_{Ir-O} for the first meta-oxygen shell Ir-O in the sample prepared by the A-synthesis as function of potential cycle number.

oxidized to a higher oxide which immediately becomes hydrated, the so-called hydrated surface oxide layer. This layer hinders further oxidation of the inner oxide, and will thus limit the formation of hydrated oxide to only one monolayer for each potential cycle. At low potential the hydrated oxide becomes a hydrous oxide. To obtain more hydrous oxide, the compact oxide must be continually reduced to elemental iridium metal and be reformed by potential cycling. During reduction the hydrated surface oxide layer is released to the bulk hydrous Ir oxide, which is bound to the electrode by weak electrostatic forces and van der Waals forces. Processes such as hydrogen adsorption and desorption at the surface of elemental iridium metal are therefore not affected by the presence of the hydrated bulk hydrous oxide layer. At the boundary between the elemental metal and the bulk hydrous oxide the monolayer of hydrated oxide layer is released to the hydrous bulk oxide, which accumulates after each cycle. Essential to oxide growth is therefore the reduction to elemental iridium metal, and unless the lower vertex potential is sufficiently low, growth will not occur. Similar dependence of oxide growth on the lower potential boundary was seen for the sample studied in this work (Fig. 3), where a lower potential boundary of 0.2 V resulted in no growth of the oxide peaks in the voltammogram.

We also note that although X-ray induced oxidization of the samples in an electrolyte is a challenging factor for in-situ/operando experiments, our electrochmemistry results indicate that this is not a significant factor in our case. Comparison of the cyclic voltammograms recorded ex situ (Fig. 2(a)) and those recorded in situ (Fig. 5) are reasonably similar. This indicates that the samples are oxidised to a degree independent of the exposure to X-rays.

The growth on the PPS Ir powder levels off after approximately 60 cycles, Fig. 3. This can also be explained within the mechanism of Pickup and Birss as above. The same evolution with ceasing signal in this potential area was seen for a sol-gel film containing 2 nm metallic Ir nanoparticles[48]. Here a steady-state anodic charge was also developed after a certain number of cycles, which was in contrast to the oxidation of Ir metal wire studied for comparison[48]. For the Ir wire the mirror-image peak at 0.97 V continued to increase. Disappearing hydrogen adsorption/desorption peaks for the films with nanoparticles of metallic Ir were also seen, and was proposed to be a result of either complete oxidation of the metallic Ir, or be due to formation of the hydrous iridium oxide film blocking the underlying metallic Ir. In our case the first explanation does not apply as presence of metallic Ir was verified by in situ XAS measurements (Fig. 10). The second on the other hand might be applicable, and may explain the ceasing growth of the Ir(+3)/Ir(+4) peaks and the disappearing H-adsorption peak as function of potential cycling. As reported by Pickup and Birss[47] oxidation may cease after some cycles if the low potential boundary is not set at a sufficiently low potential. Also, if the reduction of the inner oxide is not completed it will build up and hinder the H-adsorption process[47]. The lower potential boundary was therefore set low enough for some oxidation to occur, however, not low enough for complete reduction for every cycle.

The disappearance of the hydrogen peaks upon cycling is therefore likely to be related to the electronic structure of the oxide continously forming on the elemental iridium metal substrate. The electronic structure of AIROF appears to be that of a semiconductor in the reduced state (reaction (2) shifted to the right) and conducting in the oxidised (reaction (2) shifted to the left)[27,58]. A direct measurement of this transition from in-situ conductivtiy and scanning-probe measurements was reported by Ilyukhina *et al.*[26] for electrochemically formed iridium oxide (EIROF). The H-UPD region would appear at potentials at which the oxide is reduced and thus semiconducting. The flatband potential of AIROF is approximately 800 mV in solutions of sulfuric acid at pH 0.4[57], and the oxide behaves as a p-type conductor. This means the energy levels associated with the hydrogen reaction may not straddle the valence band edge, and if so that the H-UPD cannot take place[59]. Therefore, as the elemental metal transforms to oxide

Published on 30 March 2020. Downloaded by University of Southampton on 3/31/2020 1:02:17 PM.
Physical Chemistry Chemical Physics Accepted Manuscript

This journal is © The Royal Society of Chemistry [year]

View Article Online
DOI: 10.1039/D0CP00217H

Published on 30 March 2020. Downloaded by University of Southampton on 3/31/2020 1:02:17 PM.

the H-UPD peaks vanish.

For oxides formed by chemical methods (PPS or hydrolysis) a voltammetric response in the H-UPD potential is frequently observed, although rarely as pronounced as in Fig. 2(b) (cycle 150) and sometimes difficult to separate from the balance of the voltammogram altogether[15,18,32,60–62]. Some of these oxides, such as those prepared by hydrolysis[27,63], appear to lack the conductivity-switching ability of AIROF and EIROF. They therefore behave as metals at all potentials, and a H-UPD process appears more or less well separated from the intercalation process, Eq. (2).

As far as the distribution of metal and oxide phases is concerned TEM images remain inconclusive, and other methods for the analysis such as those undertaken above are clearly warranted. Some of the TEM images (Fig. S.5 in the ESI) did indicate the presence of some IrO_2 (lattice fringes 3.2 – 3.3 Å apart, compatible with the iridium-iridium distance in IrO_2, shell 3 (Ir-Ir,Ox1)), but these were not the dominating feature of the images. Also, as the parts of the samples most accessible to oxygen are presumably also be those most accessible to the electron beam, this may lead to misinterpretation. In view of the possibilities for performing in-situ measurements and probing larger parts of the sample XANES and EXAFS have been demonstrated in this work to be decisive in determining the structure of the catalyst manufactured by the PPS method.

The *corrected* multiplicity of the three metal shells were all smaller than the reference values (see Fig. S3 in the ESI), which indicates the presence of small particles[64]. For Pt metal particles the reduction in multiplicity is expected to be significant below 5 nm[64]. Thus, our values for the corrected multiplicity indicate that (elemental) metallic Ir crystallites of a size less than 5 nm are present. The crystallite size obtained by XRD, on the other hand, indicates a crystallite size much larger than this. However, XRD has difficulties in probing the structure of crystallites smaller than about 5 nm in size since the Bragg peaks get very broad[28]. XAS on the other hand probes the local atomic environment, and there is no lower size limit with respect to crystallite size in terms of what is detected. In that way XRD and EXAFS are not probing crystallite sizes at an overlapping scale, and any difference observed between the two techniques can be caused by this fact. It is therefore likely that the size distribution is rather wide or bimodular.

5 Conclusions

Iridium oxides prepared by PPS possess surface areas of $> 1\ m^2\ g^{-1}$ and appear to be very interesting for electrocatalytic purposes. However, a sufficient oxygen supply during the synthesis is decisive for avoiding the formation of elemental iridium metal. PPS-produced iridium powder prepared without taking the necessary precautions with respect to the oxygen supply during the heat treatment will result in a mix of iridium elemental metal and oxide phase. The surface of this elemental iridium metal may be oxidised to anodic iridium oxide films by electrochemical cycling, as observed from increasing Ir(+3)/Ir(+4) peaks, similar to those of anodic iridium oxide films, with cycle number and disappearing hydrogen adsorption/desorption peaks.

From in situ XAS measurements we have inferred that the post-synthesis treatment by potential cycling only oxidises a thin layer of the elemental component of the elemental iridium-iridium oxide composite and that only an insignificant oxidation of the elemental metal fraction occurred over the course of potential cycling. The addition of trivalent Ir in the LCF of XANES revealed the possibility of trivalent Ir in the structure, accounting for an estimated 7 at.% after heat treatment. Upon potential cycling this fraction decreased to 2 at.%. Excluding the trivalent state in the LCF a 4.7 at.% decrease of the fraction of elemental iridium metal was found. The emergence and growth of peaks associated with the oxidation of Ir(+3) to Ir(+4) in AIROF, the saturation of this growth after approximately 60 cycles, the disappearance of hydrogen adsorption/desorption peaks as function of potential cycling, and the reversibility upon drying of the electrode can be explained from the mechanism of oxide growth on AIROF and its electronic properties.

The preparation of PPS appears particularly attractive in applications in which the oxide can be heat-treated in situ on a conducting support, for example as an alternative to DSA electrodes. Under these conditions the oxygen supply may be sufficient for a complete formation of iridium oxide from the precursors. For applications in which the oxide is to be dispersed on a polymeric substrate, for example for catalyst-coated membranes in PEM electrolysers, the oxide has to be prepared in bulk. Under these circumstances precautions to ensure a sufficient oxygen supply during synthesis will have to be taken, since any post-synthesis eletrochemical treatment will have limited effect and leave substantial parts of the iridium in oxidation state zero at the interior of the material and therefore inactive.

Conflicts of interest

There are no conflicts to declare.

Acknowledgements

The funding for this research was provided by Faculty of Natural Sciences and Technology at NTNU (project no. 81730900), and was greatly appreciated. We thank Diamond Light Source for providing access to synchrotron beam-time on B18 (proposal 8591) and synchrotron technician Diego Gianolio for help during the recording of the X-ray absorption spectroscopy data. The authors would like to acknowledge support from the Research Council of Norway through the Norwegian Center for Transmission Electron Microscopy, NORTEM (197405/F50), and Bjørn Gunnar Soleim for performing the TEM imaging.

Notes and references

1 A. Grupioni, E. Arashiro and T. Lassali, *Electrochimica Acta*, 2002, **48**, 407 – 418.
2 D.-Q. Liu, S.-H..Yu, S.-W. Son and S.-K. Joo, *ECS Transactions*, 2008, **16**, 103–109.
3 Y.-T. Shih, K.-Y. Lee and Y.-S. Huang, *Journal of Alloys and Compounds*, 2015, **619**, 131 – 137.
4 Y. Jung, J. Lee and Y. Tak, *Electrochemical and Solid-State Letters*, 2004, **7**, H5–H8.

Physical Chemistry Chemical Physics Accepted Manuscript

View Article Online
DOI: 10.1039/D0CP00217H

Published on 30 March 2020. Downloaded by University of Southampton on 3/31/2020 1:02:17 PM.

5 W.-D. Huang, H. Cao, S. Deb, M. Chiao and J. Chiao, *Sensors and Actuators A: Physical*, 2011, **169**, 1 – 11.

6 P. Steegstra and E. Ahlberg, *J. Electroanal. Chem.*, 2012, **685**, 1–7.

7 J. Park, M. Kim and S. Kim, *Sensors and Actuators B: Chemical*, 2014, **204**, 197 – 202.

8 T. Y. Kim and S. Yang, *Sensors and Actuators B: Chemical*, 2014, **196**, 31 – 38.

9 M. Carmo, D. L. Fritz, J. M. Mergel and D. Stolten, *International Journal of Hydrogen Energy*, 2013, **38**, 4901 – 4934.

10 E. Fabbri, A. Habereder, K. Waltar, R. Kotz and T. J. Schmidt, *Catal. Sci. Technol.*, 2014, **4**, 3800–3821.

11 S. Negi, R. Bhandari, L. Rieth, R. V. Wagenen and F. Solzbacher, *J. Neuroscience Methods*, 2010, **186**, 8–17.

12 V. Birss, R. Myers, H. Angerstein-Kozlowska and B. E. Conway, *Journal of The Electrochemical Society*, 1984, **131**, 1502–1510.

13 T. Pauporté, D. Aberdam, J.-L. Hazemann, R. Faure and R. Durand, *Journal of Electroanalytical Chemistry*, 1999, **465**, 88 – 95.

14 A. R. Hillman, M. A. Skopek and S. J. Gurman, *Physical Chemistry Chemical Physics (Incorporating Faraday Transactions)*, 2011, **13**, 5252.

15 L.-E. Owe, M. Tsypkin, K. S. Wallwork, R. G. Haverkamp and S. Sunde, *Electrochimica Acta*, 2012, **70**, 158 – 164.

16 A. Skulimowska., M. Dupont, M. Zaton, S. Sunde, L. Merlo, D. J. Jones and J.Rozìre, *International Journal of Hydrogen Energy*, 2014, **39**, 6307–6316.

17 A. Zlotorowicz, S. Sunde and F. Seland, *International Journal of Hydrogen Energy*, 2015, **40**, 9982 – 9988.

18 A. de Oliveira-Sousa, M. da Silva, S. Machado, L. Avaca and P. de Lima-Neto, *Electrochimica Acta*, 2000, **45**, 4467 – 4473.

19 E. Rasten, G. Hagen and R. Tunold, *Electrochimica Acta*, 2003, **48**, 3945 – 3952.

20 E. Mayousse, F. Maillard, F. Fouda-Onana, O. Sicardy and N. Guillet, *International Journal of Hydrogen Energy*, 2011, **36**, 10474 – 10481.

21 S. Siracusano, N. V. Dijk, E. Payne-Johnson, V. Baglio and A. Aricó, *Applied Catalysis B: Environmental*, 2015, **164**, 488 – 495.

22 L.-E. Owe, M. Tsypkin and S. Sunde, *Electrochimica Acta*, 2011, **58**, 231 – 237.

23 M. A. Petit and V. Plichon, *Journal of Electroanalytical Chemistry*, 1994, **379**, 165–172.

24 S. Gottesfeld, J. McIntyre, G. Beni and J. Shay, *Appl. Phys. Lett.*, 1978, **33**, 208–210.

25 S. Gottesfeld and J. McIntyre, *J. Electrochem. Soc.*, 1979, **126**, 742–750.

26 L. Ilyukhina, S. Sunde and R. G. Haverkamp, *J. Electrochem. Soc.*, 2017, **164**, F1662–F1670.

27 I. A. Lervik, M. Tsypkin, L.-E. Owe and S. Sunde, *Journal of Electroanalytical Chemistry*, 2010, **645**, 135 – 142.

28 M. Hüppauff and B. Lengeler, *Journal of The Electrochemical Society*, 1993, **140**, 598–602.

29 H. Nong, L. Gan, E. Willinger, D. Teschner and P. Strasser, *Chemical Science*, 2014, **5**, 2955–2963.

30 H. Nong, H.-S. Oh, T. Reier, E. Willinger, M.-G. Willinger, V. Petkov, D. Teschner and P. Strasser, *Angewandte Chemie - International Edition*, 2015, 2975 – 2979.

31 P. Strasser and S. Kuehl, *Nano Energy*, 2016, **29**, 166–177.

32 A. H. Reksten, A. E. Russell, P. W. Richardson, S. J. Thompson, K. Mathisen, F. Seland and S. Sunde, *Phys. Chem. Chem. Phys.*, 2019, **21**, 12217–12230.

33 S. Gottesfeld and J. McIntyre, *J. Electrochem. Soc.*, 1979, **126**, 742–750.

34 A. Terezo and E. Pereira, *Electrochimica Acta*, 2000, **45**, 4351–4358.

35 A. J. Terezo and E. C. Pereira, *Materials Letters*, 2002, **53**, 339–345.

36 M. Santos, A. Terezo, V. Fernandes, E. Pereira and L. Bulhões, *Journal of Solid State Electrochemistry*, 2005, **9**, 91–95.

37 A. V. Rosario, L. O. Bulhoes and E. C. Pereira, *Journal of Power Sources*, 2006, **158**, 795 – 800.

38 L. Profeti, F. Simões, P. Olivi, K. Kokoh, C. Coutanceau, J.-M. Léger and C. Lamy, *Journal of Power Sources*, 2006, **158**, 1195 – 1201.

39 N. Mamaca, E. Mayousse, S. Arrii-Clacens, T. Napporn, K. Servat, N. Guillet and K. Kokoh, *Applied Catalysis B: Environmental*, 2012, **111-112**, 376 – 380.

40 D. Von Dreifus, A. J. A. de Oliveira, A. V. do Rosario and E. C. Pereira, *Journal of Superconductivity and Novel Magnetism*, 2013, **26**, 2319–2321.

41 *DIFFRAC^{plus} TOPAS 4.2 Technical Reference*, Bruker AXS GmbH. technical report, 2009.

42 T. J. Schmidt, H. A. Gasteiger, G. D. Stäb, P. M. Urban, D. M. Kolb and R. J. Behm, *J. Electrochem. Soc.*, 1998, **145**, 2354–2358.

43 B. Ravel and M. Newville, Physica Scripta T, 2005, pp. 1007–1010.

44 S. Tomic, B. Searle, A. Wander, N. Harrison, A. Dent, J. Mosselmans and J. Inglesfield, *New Tools for the Analysis of EXAFS: The DL EXCURV Package*, Council for the central laboratory of the research councils technical report, 2005.

45 T. Arikawa, Y. Takasu, Y. Murakami, K. Asakura and Y. Iwasawa, *Journal of Physical Chemistry B*, 1998, **102**, 3736–3741.

46 D. Rand and R. Woods, *Journal of Electroanalytical Chemistry and Interfacial Electrochemistry*, 1974, **55**, 375 – 381.

47 P. Pickup and V. Birss, *Journal of Electroanalytical Chemistry*, 1987, **220**, 83–100.

48 V. I. Birss, H. Andreas, I. Serebrennikova and H. Elzanowska, *Electrochemical and Solid-State Letters*, 1999, **2**, 326–329.

49 R. Kawar, P. Chigare and P. Patil, *Applied Surface Science*, 2003, **206**, 90 – 101.

50 O. Gencyilmaz, F. Atay and I. Akyuz, *Journal of optoelectronics and advanced materials*, 2015, **17**, 395–402.

51 M.-S. Miao and R. Seshadri, *Journal of Physics: Condensed Matter*, 2012, **24**, 215503.

52 J. H. A. Martens, R. Prins and D. C. Koningsberger, *The Journal of Physical Chemistry*, 1989, **93**, 3179–3185.

Physical Chemistry Chemical Physics Accepted Manuscript

This journal is © The Royal Society of Chemistry [year]

View Article Online
DOI: 10.1039/D0CP00217H

53 C. Nordhei, A. Ramstad and D. Nicholson, *Physical Chemistry Chemical Physics*, 2008, **10**, 1053–1066.

54 V. Birss, C. Bock and H. Elzanowska, *Canadian Journal of Chemistry — Revue Canadienne de Chimie*, 1997, **75**, 1687–1693.

55 B. Wessling, A. Besmehn, W. Mokwa and U. Schnakenberg, *J. Electrochem. Soc.*, 2007, **154**, F83 – F89.

56 P. Pickup and V. Birss, *Journal of the Electrochemical Society*, 1988, **135**, 126 – 133.

57 L.-E. Owe, I. A. Lervik, M. Tsypkin, M. V. Syre and S. Sunde, *J. Electrochemc. Soc.*, 2010, **157**, B1719–B1725.

58 S. Gottesfeld, *J. Electrochem. Soc.*, 1980, **127**, 1922–1925.

59 S. Cherevko, S. Geiger, O. Kasiana, A. Mingers and K. J. Mayrhofer, *J. Electroanal. Chem.*, 2016, **774**, 102–110.

60 F. Mattos-Costa, P. De Lima-Neto, S. Machado and L. Avaca, *Electrochimica Acta*, 1998, **44**, 1515–1523.

61 J. Cheng, H. Zhang, G. Chen and Y. Zhang, *Electrochimica Acta*, 2009, **54**, 6250 – 6256.

62 E. Kuznetsova, A. Cuesta, M. Thomassen and S. Sunde, *Journal of Electroanalytical Chemistry*, 2014, **728**, 102–111.

63 S. Sunde, I. A. Lervik, M. Tsypkin and L.-E. Owe, *Electrochimica Acta*, 2010, **55**, 7751 – 7760.

64 J. de Graaf, A. J. van Dillen, K. de Jong and D. Koningsberger, *Journal of Catalysis*, 2001, **203**, 307 – 321.

Published on 30 March 2020. Downloaded by University of Southampton on 3/31/2020 1:02:17 PM.

Physical Chemistry Chemical Physics Accepted Manuscript